Applied Clay Science 83–84 (2013) 68–76

Contents lists available at ScienceDirect

Applied Clay Science

journal homepage: www.elsevier.com/locate/clay

Research paper

From platy kaolinite to aluminosilicate nanoroll via one-step delamination of kaolinite: Effect of the temperature of intercalation

Peng Yuan [a,*], Daoyong Tan [a,b], Faïza Annabi-Bergaya [c], Wenchang Yan [d], Dong Liu [a], Zongwen Liu [e]

[a] CAS Key Laboratory of Mineralogy and Metallogeny, Guangzhou Institute of Geochemistry, Chinese Academy of Sciences, Guangzhou 510640, China
[b] University of the Chinese Academy of Sciences, Beijing 100039, China
[c] Centre de Recherche sur la Matière Divisée, CNRS-Université d'Orléans, 1B, rue de La Férollerie, 45071 Orléans, France
[d] School of Civil Engineering, Anhui University of Architecture, Hefei 230022, China
[e] Australian Centre for Microscopy and Microanalysis, The University of Sydney, NSW 2006, Australia

ARTICLE INFO

Article history:
Received 1 May 2013
Received in revised form 2 August 2013
Accepted 17 August 2013
Available online 10 September 2013

Keywords:
Aluminosilicate nanoroll
Kaolinite
Halloysite
Intercalation
Delamination
Thermal stability

ABSTRACT

Aluminosilicate nanorolls were prepared using a method of one-step delamination of kaolinite. In this method, cetyltrimethylammonium chloride (CTMACl) was intercalated into the interlayer space of methoxy-modified kaolinite, which resulted in the delamination and rolling of kaolinite layers. The reaction conditions of CTMACl intercalation significantly influenced the formation of nanorolls, as shown by characterizations using X-ray diffraction, electron microscopy, infrared spectroscopy, thermal analysis, and nitrogen adsorption. Overall, increasing the CTMACl-intercalation temperature helps to promote the transformation from platy kaolinite to nanorolls. The initial kaolinite particles were mostly transformed to nanorolls in the product prepared at 80 °C, whereas considerable kaolinite particles remained untransformed in the product prepared at 30 °C. At 80 °C, the obtained specific surface area (SSA) and the porous volume (V_{por}) values of the nanoroll product are nearly twice the values obtained at 30 °C and the tubular structure exhibits higher thermal persistence. The tubular morphology and the porosity of these nanorolls obtained at 80 °C, were largely retained after calcination at 600–800 °C. However, a calcination at 900 °C led to an obvious distortion of the nanorolls and a decrease in SSA and V_{por} values. The observed structural changes of the nanorolls under calcination generally resembled that of natural halloysite but occurred at lower temperatures because the prepared nanorolls were of lower structural order with thinner tube walls.

1. Introduction

Naturally occurring aluminosilicate minerals with nanosized tubular structures, such as halloysite ($Al_2(OH)_4Si_2O_5 \cdot 2H_2O$) and imogolite, have drawn the attention of researchers in the fields of adsorption, catalysis, and clay polymer nanocomposite (CPN) over the past two decades (Joussein et al., 2005; Lvov et al., 2008). Halloysite has received particular attention because of its unique tubular structure on the mesoporous (2–50 nm) and even macroporous (>50 nm) scale (Churchman et al., 1995). Halloysite is a hydrated polymorph of kaolinite with a layer of water molecules between the 1:1 aluminosilicate layers, and nanoscale tubular halloysite is the dominant form of natural halloysite. The multilayer halloysite nanotube results from the wrapping of the clay mineral layers under favorable geological conditions. This wrapping is driven by a mismatch between the oxygen-sharing tetrahedral SiO_4 sheet and its adjacent octahedral $A1O_6$ sheet in the 1:1 layer (Bates et al., 1950; Singh, 1996). Because of its unique one-dimensional mesoscopic/macroscopic porous structure and economic viability, halloysite has been applied as a nanoscale reactor (Shchukin et al., 2005), as a nanofiller for CPN (Hedicke-Hochstotter et al., 2009; Li et al., 2008a), and as a carrier or support for the entrapment and controlled release of functional guests (Levis and Deasy, 2002; Lvov et al., 2008; Tan et al., 2013; Yuan et al., 2012a). It is worth emphasizing that halloysite has a high level of biocompatibility and low cytotoxicity, which enables its safe use in various fields (Van Oss et al., 1999; Vergaro et al., 2010).

Halloysite deposits have been found in Australia, America, China, New Zealand, Mexico, and Brazil (Joussein et al., 2005). These deposits are generally found in the vicinity of kaolinite deposits and are thus mined in large volume for the ceramics industry. The yield of halloysite is much lower than the huge production of kaolinite. Moreover, natural halloysite often contains impurity phases and varies in morphology with different deposits (Pasbakhsh et al., 2013). In general, halloysite nanotubes vary in length from submicron to several microns, sometimes even >30 μm (Joussein et al., 2005), in external diameter from approximately 30 to 190 nm, and in internal diameter from approximately 10 to 100 nm (Yuan et al., 2008). The morphological properties – length, external diameter, internal diameter, and wall thickness – of halloysite significantly affect its performance in the interface reaction with functional guests (Zhou

* Corresponding author at: Guangzhou Institute of Geochemistry, Chinese Academy of Sciences, No. 511 Kehua Street, Tianhe District, Guangzhou, 510640, China. Tel.: +86 20 85290341; fax: +86 20 85290130.
E-mail address: yuanpeng@gig.ac.cn (P. Yuan).

0169-1317/$ – see front matter © 2013 Elsevier B.V. All rights reserved.
http://dx.doi.org/10.1016/j.clay.2013.08.027

and Keeling, 2013). For example, a previous study demonstrated that the quantity of hydroxyl groups of halloysite available for organosilane grafting is highly dependent on its morphological parameters (Yuan et al., 2008). Under the same pretreatment conditions, a halloysite sample with good tubule quality and uniform morphology exhibits much better silylation activity than a sample with low tubular quality. This result suggests that tubule qualities are important for the industrial uses of halloysite and that these uses are substantially limited by the diverse quality of natural halloysites sourced from different deposits.

Some efforts have been made to synthesize high-quality halloysite-like nanotubes during the last decades (Gardolinski and Lagaly, 2005; Kuroda et al., 2011). As high-quality kaolinite is readily available at low cost, one of the most attractive methods for synthesizing aluminosilicate nanotubes is based on the delamination and rolling of kaolinite layers. This process might have drawn inspiration from the observation of the kaolinite–halloysite transformation occurring in nature. For example, Giese (1988) reported that kaolinite formed from mica by topotactic alteration could subsequently produce halloysite. Singh and Gilkes (1992) described the electron-optical observation of the alteration of kaolinite plates by fragmentation into laths that rolled to form halloysite tubes. Bobos et al. (2001) confirmed the kaolinite to halloysite transformation by comparing the clay samples selected from the same geological profile in a Portuguese kaolin deposit. The theoretical studies on the rolling mechanisms of halloysite have further accelerated improving the methods for halloysite preparation.

It is widely accepted that the rolling of halloysite is driven by the lateral misfit of the smaller octahedral and larger tetrahedral sheet (Bailey, 1989; Bates et al., 1950). However, researchers were once confused as to why tetrahedral rotation – a mechanism evident in kaolinite and many 2:1 planar clay minerals that reduces the dimensions of the tetrahedral sheet – does not occur in halloysite (Giese, 1988). To address this knowledge gap, Singh (1996) proposed a theoretical model that compared the forces in the tetrahedral sheet that oppose tetrahedral rotation and rolling. The simulation results showed that the rolling dynamic encounters considerably less opposition than tetrahedral rotation in correcting for the same amount of misfit when there is no strong interlayer hydrogen bonding. Thus, the rolling mechanism is energetically more favorable than tetrahedral rotation for halloysite to accommodate the lateral misfit, and its occurrence does not depend on the cessation of tetrahedral rotation, as proposed by Bailey (1989). Singh also suggests that a planar kaolinite layer will roll after interlayer hydrogen bonding is weakened by the hydration and expansion of the interlayer space. Subsequently, Singh and Mackinnon (1996) experimentally demonstrated the formation of halloysite-like nanosized tubes through the use of repeated intercalation and deintercalation of kaolinite using potassium acetate. Gardolinski and Lagaly (2005) proposed a method for the transformation from platy kaolinite to halloysite-like nanotubes with high transformation efficiency. Kaolinite was first interlayer-grafted with alkanols, diols, and glycol mono-ethers and intercalated with n-alkylamines; the obtained intercalation compound was then delaminated in toluene, which was accompanied by the deintercalation of the amine molecules. Thin kaolinite particles rolled into a halloysite-like morphology but with much smaller tubes. Based on this method, Matusik et al. (2009) investigated the effect of the structural order of parent kaolinite on the formation of halloysite-like nanotubes. These researchers found that the production of nanotubes depends primarily on the efficiency of the interlayer modification and of the low crystallinity of the kaolinite. In designing clay nanohybrid materials in which monodispersed kaolinite-bearing functional groups homogeneously dispersed in a polymeric matrix, Letaief and Detellier (2009) proposed a method for the delamination of kaolinite. This procedure was carried out by the reaction of sodium polyacrylate with kaolinite, whose internal aluminol surfaces were previously grafted with triethanolamine and subsequently quaternized with iodomethane to form an extended lamellar inorganic polycation. The delamination causes a partial folding of the delaminated kaolinite layers, which form curved structures. These products are more precisely defined as nanorolls rather than nanotubes. Then, "nanoroll" is the term that will be used hereafter in this paper.

The preparation of halloysite-like aluminosilicate nanorolls through the delamination and rolling of kaolinite was further developed by Kuroda et al. (2011) in a simple one-step method. In this method, quaternary ammonium salts were intercalated into the interlayer space of methoxy-modified kaolinite, leading to the swelling of the intercalation compound and the concurrent transformation of platy kaolinite to nanorolls. In this one-step route for the preparation of aluminosilicate nanorolls, the intercalation reaction temperature may be an important factor affecting the interaction between the quaternary ammonium salts and the interlayer surface of kaolinite. It has been reported that the reaction temperature has significant effects on the behavior of clay minerals (Elaouar, 1962) and on the structure of intercalated organoclays, such as organosilane-modified kaolinite (Yang et al., 2012). However, the effects of the intercalation reaction temperature on the transformation from platy kaolinite into halloysite-like nanorolls, which is important for optimizing the preparation parameters for practical use and for deepening the understanding of organic guests–clay interaction, were not investigated.

In the present work, methoxy-modified kaolinite was prepared as the initial material for intercalation with cetyltrimethylammonium chloride ($C_{16}H_{33}(CH_3)_3NCl$, CTMACl). Series intercalation reaction temperatures ranging from 30 to 100 °C were applied for the intercalation reactions. The transformations from kaolinite to halloysite-like nanorolls under different reaction temperatures were carefully compared, and the related interaction mechanisms between the kaolinite host and the organic guests were investigated. The thermal stability of the produced aluminosilicate nanoroll was also well characterized.

2. Experimental section

2.1. Materials and methods

A kaolinite specimen (denoted hereafter as Kaol) with high purity, obtained from Maoming Guangdong Province, China, was used as received without further purification. The chemical composition of Kaol, as determined from chemical analysis in percent by mass of the respective oxide form, is: SiO_2, 46.75; Al_2O_3, 39.15; Fe_2O_3, 1.02; MgO, 0.10; CaO, 0.21; K_2O, 0.25; Na_2O, 0.26; MnO, 0.01; TiO_2, 0.32; P_2O_5, 0.04; and loss on ignition, 11.92. Dimethyl sulfoxide (DMSO), isopropanol, 1, 4-dioxane, ethanol, and methanol (MeOH) were purchased from Sinopharm Chemical Reagent Co., Ltd., and CTMACl was from Nanjing Robiot Co., Ltd.. All of these reagents were of analytical grade purity (>99.0%) and used as received.

To prepare the DMSO-intercalated Kaol, 10.0 g of Kaol was added into a mixture of 60 mL DMSO and 10 mL distilled water. The resultant dispersion was then stirred and refluxed at 150 °C for 12 h, followed by aging at room temperature (approximately 25 °C) for 12 h. The solid in the mixture was separated by centrifugation and washed 3 times by using 1,4-dioxane and isopropanol to eliminate the excess DMSO. The product was dried at 60 °C for 24 h and then ground into powder for further use. The DMSO-intercalated Kaol was denoted Kaol–DMSO.

To prepare the methoxy-modified Kaol, 5.0 g of Kaol–DMSO was added into 100 mL MeOH and stirred for 7 days. The solid in the mixture was separated by centrifugation and stored in a wet state for further use; it was denoted Kaol–MeOH(wet). A part of the Kaol–MeOH(wet) was dried at 60 °C for 24 h. The dried product was denoted Kaol–MeOH(dry).

To prepare the aluminosilicate nanoroll, approximately 1.0 g of Kaol–MeOH(wet) was added into a 40 mL MeOH solution of CTMACl 1 M and stirred under different reaction temperatures (30–100 °C) for 24 h. The solid in the mixture was separated by centrifugation, extensively washed 6 times with fresh ethanol to remove the CTMACl in excess, and then dried at 80 °C for 24 h. The product was denoted Kaol–

CTMACl-X, where X was the value, in degrees Celsius, of the reaction temperature. A part of the wet-state solid product that did not undergo ethanol washing was left for further characterizations, and the related product was denoted by adding the suffix '(unwashed)' to the name of the ethanol-washed sample, for example, Kaol–CTMACl-30(unwashed).

To prepare the calcination treatment of the aluminosilicate nanoroll products, portions of the products were heated in a programmed temperature-controlled muffle furnace at scheduled temperatures (600–900 °C) for 2 h. The products were ground into powders in an agate mortar and were denoted Kaol–CTMACl-X(T), where T was the heating temperature. For example, Kaol–CTMACl-30(600 °C) refers to the aluminosilicate nanoroll product for which the reaction temperature was 30 °C and the heating temperature was 600 °C.

2.2. Characterization techniques

The X-ray diffraction (XRD) patterns were recorded on a Bruker D8 Advance diffractometer with Ni filter and Cu K_α radiation ($\lambda = 0.154$ nm) generated at 40 kV and 40 mA. The scan rate was 1°(2θ)/min. Transmission electron microscopy (TEM) observations were conducted on a 200 kV JEOL JEM-2100 high-resolution transmission electron microscope. The specimens were prepared as follows: the clay mineral or the heated product powder was ultrasonically dispersed in ethanol for 5 min, and then a drop of the dispersion was deposited onto a carbon-coated copper grid, which was left to stand for 10 min before being transferred into the microscope. The micrographs of scanning electron microscopy (SEM) were obtained with a 5 kV FEI-Sirion 200 field-emission scanning electron microscope.

N_2 adsorption–desorption isotherms were determined with a Micromeritics ASAP 2020 system at boiling nitrogen temperature. Sample powders were outgassed at 150 °C for 12 h before measurement. The specific surface area (SSA) of the powder was calculated by the multiple-point Brunauer–Emmett–Teller method (Gregg and Sing, 1982), and the total porous volume (V_{por}) was evaluated from nitrogen uptake at a relative pressure of about 0.99. The non-local density functional theory (NLDFT) method was used to calculate the pore size distribution (PSD) curve from the desorption isotherms (Lowell et al., 2004).

Diffuse reflectance infrared Fourier transform (DRIFT) spectra in the hydroxyl region were collected (64 scans at 2 cm^{-1} resolution) on the diffuse reflectance attachment of the Bruker Vertex 70 Fourier transform infrared spectrometer. A portion of the powder was lightly packed into a 4 mm inner diameter microsample cup for DRIFT spectra collection, and the spectra were normalized against a KBr background reference.

Thermogravimetry (TG) and differential scanning calorimetry (DSC) analyses were performed with a Netzsch STA 409PC instrument. Approximately 10 mg of sample powder was heated in a platinum crucible from 30 °C to 1300 °C at a rate of 10 °C/min under a highly pure N_2 atmosphere (60 cm^3/min).

3. Results and discussion

3.1. Characterizations of the intermediate and final products during aluminosilicate nanorolls preparation

3.1.1. XRD

Kaol shows a typical diffraction pattern with characteristic basal reflection of 0.71 nm (Fig. 1a). Kaol–DMSO exhibits an XRD pattern identical to that of the DMSO-intercalated Kaol previously reported (Martens et al., 2002; Raupach et al., 1987; Thompson and Cuff, 1985). The d_{001} value of Kaol–DMSO is 1.12 nm (Fig. 1b), which shows that the interlayer distance of Kaol was enlarged because of the intercalation of DMSO. The structure of DMSO-intercalated Kaol was previously discussed in the above-mentioned literature. Fig. 2a shows a schematic representation of the DMSO arrangement in the interlayer space of DMSO-intercalated Kaol (Thompson and Cuff, 1985). The oxygen of the S=O group is triply hydrogen bonded with the inner-surface hydroxyls of the gibbsite sheet of the Kaol layer, and one methyl group of DMSO is keyed into the ditrigonal hole in the tetrahedral sheet with the other S–C bond nearly parallel to the sheet. The intercalation ratio of Kaol–DMSO is 95.0%, as calculated from the equation

$$IR = I_I/(I_K + I_I),$$

where I_K and I_I are the intensities of (001) diffractions of Kaol and DMSO-intercalated Kaol, respectively (Lagaly et al., 2006).

Kaol–MeOH(wet) exhibits a (001) diffraction with a d_{001} value of 1.11 nm (Fig. 1c). This configuration indicates a typical interlayer structure of the methanol-intercalated Kaol in the wet state, which is composed of monolayer methanol molecules between the undisturbed siloxane surface and the methoxy-modified inner surface in which the initial aluminol (AlOH) groups in the interlayer space were converted to AlOMe groups (Tunney and Detellier, 1996), as depicted in Fig. 2b. The intercalation ratio of Kaol–MeOH(wet) is 93.7%, based on a

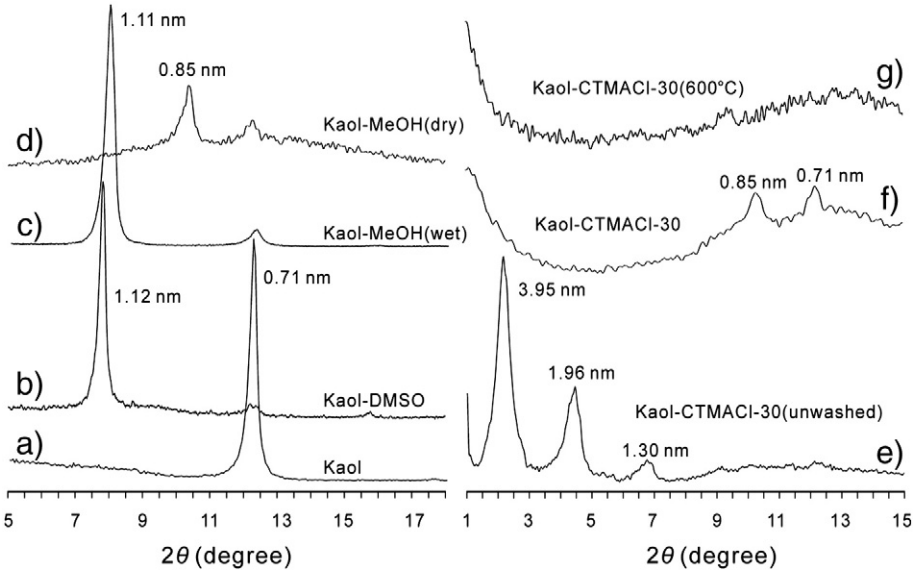

Fig. 1. XRD patterns of Kaol and the intercalated Kaol products. (a) Kaol; (b) Kaol–DMSO; (c) Kaol–MeOH(wet); (d) Kaol–MeOH(dry); (e) Kaol–CTMACl-30(unwashed); (f) Kaol–CTMACl-30; (g) Kaol–CTMACl-30(600 °C).

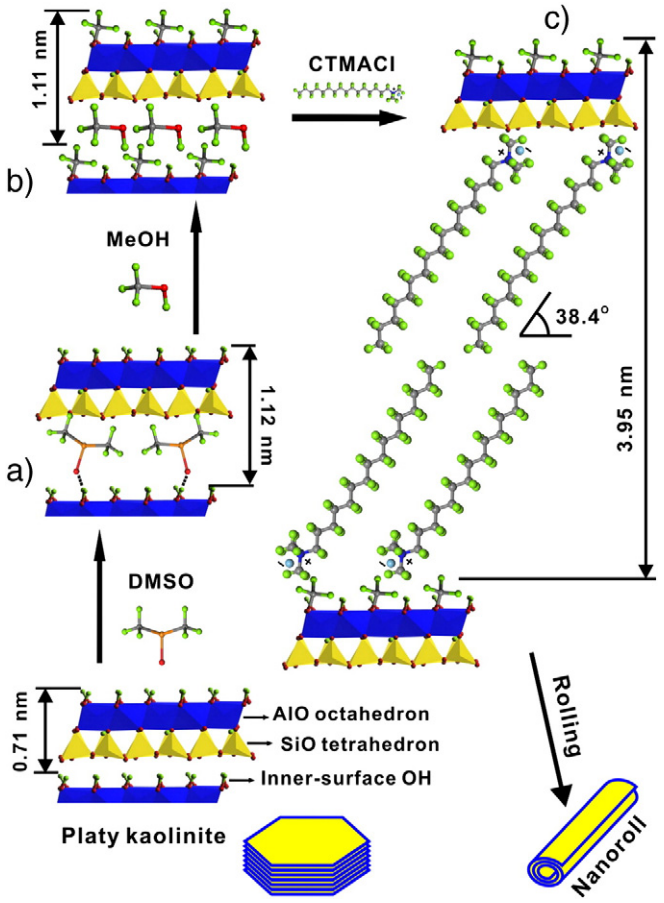

Fig. 2. Schematic representation of the transformation from platy Kaol to nanoroll.

calculation similar to that of Kaol–DMSO. The methoxy-modified inner surface resulted from the grafting of methanol molecules at the initial AlOH of the Al–O octahedron through the condensation between the hydroxyl groups of the two moieties. A small number of water molecules might also be present in the interlayer space of Kaol–MeOH(wet) because water may be generated by the grafting reaction or adsorbed from the ambient air (Komori et al., 2000). The basal reflection of Kaol–MeOH(dry), the methanol-intercalated Kaol in a dry state, is reduced to 0.85 nm (Fig. 1d). The decrease in the d_{001} value of Kaol–MeOH(dry) compared to Kaol–MeOH(wet) is caused by the escape of methanol molecules from the interlayer space during the drying process. However, a number of hydrogen-bonded methanol or water molecules were likely remained in the interlayer space of Kaol, because the d_{001} value of the partially hydrated product of methoxy-modified kaolinite is approximately 0.86 nm, whereas the d_{001} value of non-hydrated methoxy-modified kaolinite is only 0.82 nm (Komori et al., 2000; Tunney and Detellier, 1996).

In the XRD pattern (Fig. 1e) of Kaol–CTMACl-30(unwashed), the (001), (002) and (003) reflections, with d values of 3.95, 1.96, and 1.30 nm, respectively, are clearly identified, indicating the intercalation of CTMACl molecules without destroying the lamellar structure of Kaol. The intercalation ratio is approximately 96% in Kaol–CTMACl-30(unwashed). In this XRD pattern, the (001) diffraction of the initial Kaol was apparently disturbed by the diffraction of the CTMACl-intercalated Kaol (Fig. 1e). This might lower the accuracy of the calculation of intercalation ratio. Based on a stereochemical calculation that is generally used to simulate the arrangement of organic compounds in the interlayer space of clay minerals such as montmorillonite and Kaol (Kuroda et al., 2011; Lagaly, 1981), the CTMACl molecules should be arranged in the form of a tilted bilayer in the interlayer space of Kaol, and the inclination angle of the alkyl chains of CTMACl is approximately 38.4° (Fig. 2c). Notably, the actual configuration of the intercalated organic compounds is much more complicated than the ideal configuration postulated by stereochemical calculation, according to the results obtained by molecular dynamics simulation (Zeng et al., 2003). In the XRD pattern (Fig. 1f) of Kaol–CTMACl-30, a basal reflection of 0.85 nm is shown, and the overall pattern is similar to that of Kaol–MeOH(dry), which indicates that CTMACl molecules were mostly removed from the interlayer space by washing. In addition, the characteristic (001) diffraction (d = 0.71 nm) of kaolinite is still shown in the XRD pattern (Fig. 1f) of Kaol–CTMACl-30, which suggests the existence of the partial remaining untransformed Kaol.

3.1.2. TEM and SEM

As indicated by the bright-field TEM image of Kaol (Fig. 3a), the platelike Kaol particles have a typical pseudo-hexagonal morphology. Simplified as a square particle, the Kaol particles in Kaol exhibit an average size of approximately 500 × 500 ± 200 nm and an average thickness of approximately 400 ± 150 nm, according to a mean of multiple TEM images. The DMSO intercalation and MeOH modification did not change the platy morphology of Kaol (related microscopic images are not shown). However, the TEM image of Kaol–CTMACl-30(unwashed) (Fig. 3b) clearly shows the formations of nanoroll particles with typical cylindrical shapes and with transparent central lumen areas running longitudinally along the cylinder and with open ends. The relatively low contrast of the TEM image (Fig. 3b) of Kaol–CTMACl-30(unwashed) might be caused by the remaining organic compounds in the specimen affecting the microscopic resolution. The nanoroll formation in the unwashed CTMACl-modified Kaol product suggests that the swelling of the CTMACl-modified Kaol was accompanied by the delamination and rolling of Kaol layers. In the TEM image of Kaol–CTMACl-30 (Fig. 3c), the nanoroll formation is also clearly shown, which indicates that the removal of the intercalated CTMACl molecules did not reverse the rolling of the Kaol layers, although the XRD pattern of Kaol–CTMACl-30 is analogous to that of Kaol–MeOH(dry) with platy morphology.

The TEM images of Kaol–CTMACl-30 products (both unwashed and washed) show the universal existence of platy particles (Fig. 3b and c) or partially curled Kaol layers (Fig. 3d). These structures result from the incomplete delamination and rolling of the kaolinite particles. According to a mean of multiple TEM images, the nanorolls in Kaol–CTMACl-30 have an average external diameter, internal diameter, and wall thickness of approximately 26 ± 8 nm, 22 ± 8 nm, and 4 ± 2 nm, respectively; the average length of the nanorolls is approximately 150–700 nm, which is generally smaller than the lateral size of the parent Kaol. This result indicates that some of the Kaol layers are fragmented during the intercalation or delamination processes, which is supported by the TEM (Fig. 3e) and SEM (Fig. 3f) observation that small nanorolls were formed on a large parent Kaol substrate. The validity of the summary on morphological data was limited by the fact that only a very small number of nanorolls were characterized in the microscopic observation.

3.1.3. N_2 adsorption–desorption isotherms and porosity parameters

The nitrogen adsorption isotherms of Kaol (Fig. 4a) resemble type II isotherms, according to the classification used by the International Union of Pure and Applied Chemistry (IUPAC). The hysteresis loop is minor, which indicates that the mesopores resulting from the stacking of the Kaol particles are small in scale. The isotherms of Kaol–CTMACl-30 belong to type IV with H3 hysteresis loops, according to the IUPAC classification. Hysteresis loops are associated with the filling and emptying of the cylindrical mesopores of the nanorolls by capillary condensation. The PSD curves of Kaol–CTMACl-30, calculated by the NLDFT method (inset of Fig. 4a), show that primary distribution is centered at approximately 24.8 nm, which is consistent with the inner diameter of the nanorolls estimated by the TEM observations. There is also a pore size distribution ranging from 27 to 33 nm, most likely resulting from the interparticle pores. Clearly, the nitrogen adsorption–desorption technique provides a relatively complete understanding of porosity

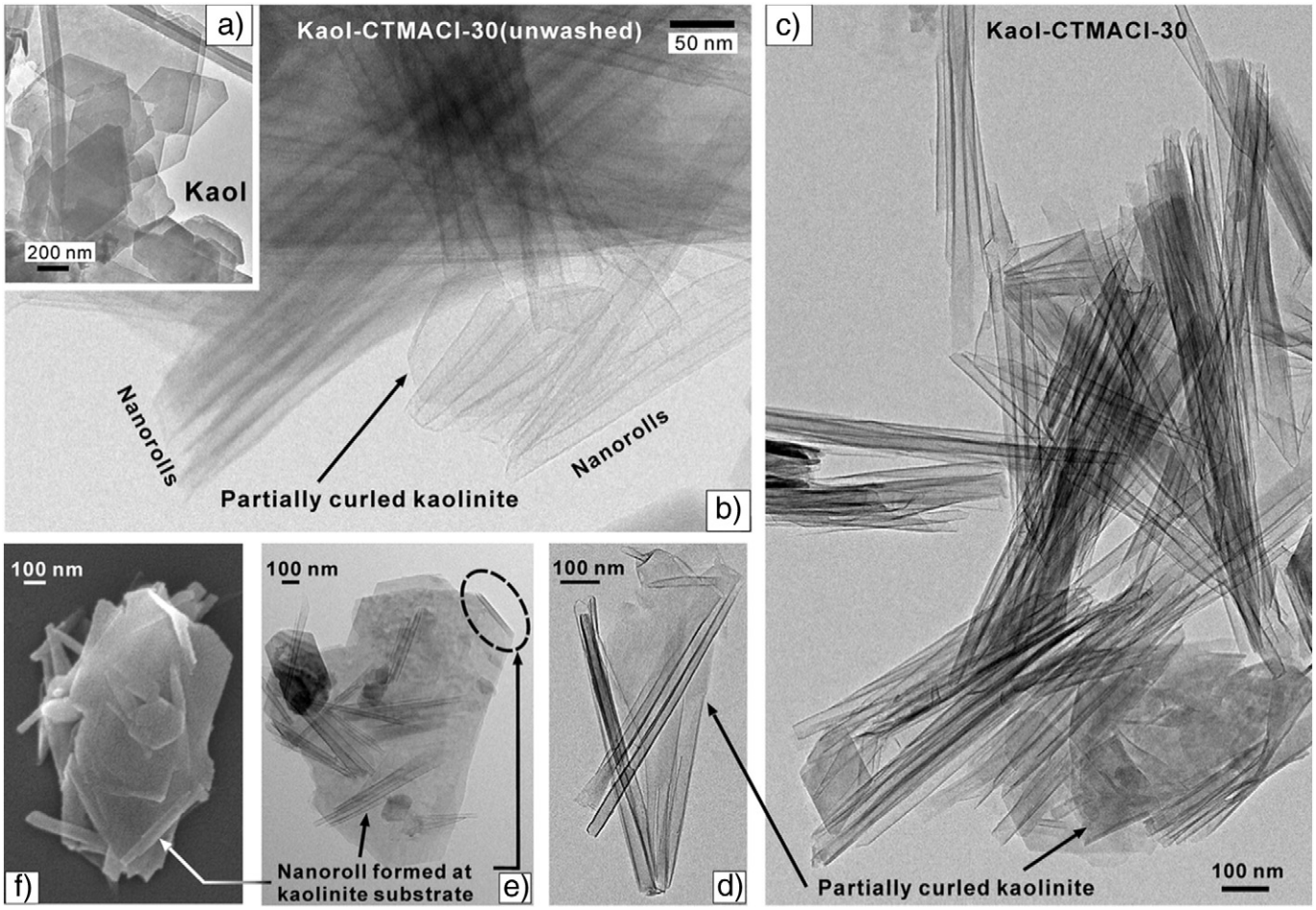

Fig. 3. Bright-field TEM images of (a) Kaol; (b) Kaol–CTMACl-30(unwashed); (c-e) Kaol–CTMACl-30; (f) SEM image of Kaol–CTMACl-30.

and represents the entire sample, so it is complementary to TEM for the porosity characterization of the produced nanorolls. The SSA and V_{por} values of Kaol–CTMACl-30 are 32.6 m^2/g and 0.17 cm^3/g, respectively; these values are substantially larger than those of Kaol (18.4 m^2/g and 0.09 cm^3/g) because one initial Kaol particle was transformed into hundreds of nanorolls via delamination and rolling, which apparently increases the surface area and the porosity of the product.

3.1.4. Drift

The DRIFT spectra of the Kaol products are shown in Fig. 5. The vibrations at 3694, 3669, and 3653 cm^{-1} in the spectrum of Kaol are ascribed to the O–H stretching of inner-surface hydroxyl groups of Kaol, and the vibration at 3621 cm^{-1} is attributed to the O–H stretching of inner hydroxyl groups (Madejova and Komadel, 2001). The major difference between the high-wavenumber region of the DRIFT spectra of Kaol (Fig. 5a)

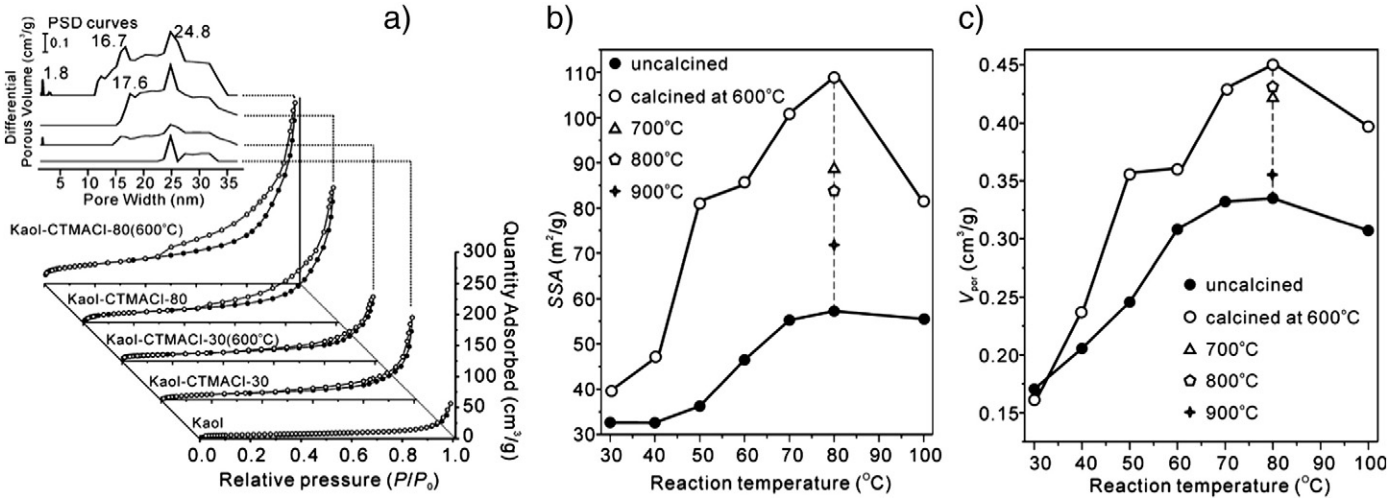

Fig. 4. (a) N_2 adsorption–desorption isotherms of Kaol and its derivate products; inset: PSD curves of nanoroll products; (b) SSA and (c) V_{por} values of the nanoroll products prepared at different intercalation reaction temperatures and calcination temperatures.

and Kaol–DMSO (Fig. 5b) is the appearance of the vibrations at 3542 and 3506 cm^{-1}, which are assigned to the bonding of the DMSO molecules with the inner-surface hydroxyl groups of the Kaol layers. Moreover, the vibrations of antisymmetric C–H stretching (3021 cm^{-1}) and symmetric C–H stretching (2936 cm^{-1}) appear, indicating the existence of DMSO molecules in Kaol–DMSO (Fig. 5b). These vibrations have been discussed in previous studies on Kaol–DMSO complexes (Frost et al., 1999; Johnston et al., 1984; Tunney and Detellier, 1996).

In the DRIFT spectrum of Kaol–MeOH(dry) (Fig. 5c), the typical vibrations of DMSO (3542 and 3506 cm^{-1}) are significantly weakened, which indicates the substitution of DMSO by methanol species. The vibrations at 3022 and 2936 cm^{-1}, in addition to those at 2848 cm^{-1}, are primarily caused by the antisymmetric and symmetric C–H stretching bands of the surface methoxy groups, respectively. These methoxy groups were formed through an alcohol condensation reaction between the methanol molecules and the inner-surface AlOH groups of Kaol, which caused the formation of Al–O–C bonds (Tunney and Detellier, 1996). The 3266 cm^{-1} band might be i) due to a high degree of polymerization of methanol molecules hydrogen bonded to each other and characterized by a frequency between 3297 and 3254 (Annabi-Bergaya et al., 1980) and ii) an indication of the small amount of methanol molecules that are hydrogen bonded with the interlayer siloxane surface, as indicated by the aforementioned XRD result. The 3550 cm^{-1} band is characteristic of hydrated kaolinite (Komori et al., 1999; Tunney and Detellier, 1994), which indicates that hydrogen bonds between OH groups of Kaol and interlayer water molecules were present. Furthermore, the OH-stretching bands of Kaol are obviously perturbed by the methanol species grafted onto the inner-surface hydroxyl groups; this response is demonstrated because the band at 3696 cm^{-1} (the O–H stretching vibration of the inner-surface hydroxyl groups) remains at roughly the same wavenumber but with an obviously weaker relative intensity, which indicates that inner-surface hydroxyl groups are being consumed during grafting.

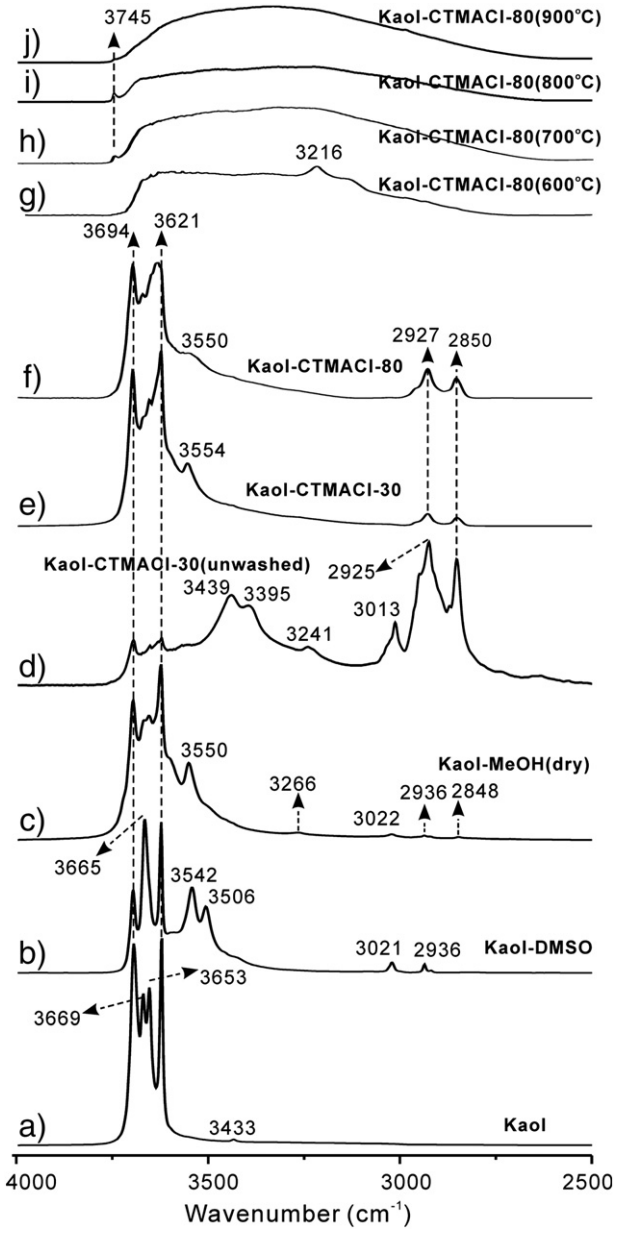

Fig. 5. DRIFT spectra of (a) Kaol; (b) Kaol–DMSO; (c) Kaol–MeOH(dry); (d) Kaol–CTMACl-30(unwashed); (e) Kaol–CTMACl-30; (f) Kaol–CTMACl-80; (g) Kaol–CTMACl-80(600 °C); (h) Kaol–CTMACl-80(700 °C); (i) Kaol–CTMACl-80(800 °C); (j) Kaol–CTMACl-80(900 °C).

In the spectrum (Fig. 5d) of Kaol–CTMACl-30(unwashed), several typical vibrations of CTMACl molecules, including 3439, 3395, 3241, and 3013 cm^{-1} (Li et al., 2008b; Rathman and Scheuing, 1990), are observed. The vibrations at 2925 and 2850 cm^{-1} can be attributed to adsorbed methanol molecules in the liquid state (Annabi-Bergaya et al., 1980). The vibrations of CTMACl are substantially decreased in the spectrum of Kaol–CTMACl-30 (Fig. 5e), which indicates that most CTMACl molecules were removed after washing. The entire spectrum of Kaol–CTMACl-30 resembles that of Kaol–MeOH(dry); however, the bands at 2927 and 2850 cm^{-1} in the spectrum of Kaol–CTMACl-30, which are attributed to the C–H stretching of the surface methoxy groups in the nanorolls (Fig. 5e), show a slight shift compared to their counterparts in the spectrum of Kaol–MeOH(dry), which is most likely caused by the disturbance of the remaining CTMACl molecules.

3.2. Effects of intercalation conditions on the structure of aluminosilicate nanorolls

The transformation from Kaol to aluminosilicate nanorolls through the delamination method is outlined (Fig. 2) on the basis of the above results. Both the interlayer modification of Kaol with methoxy groups and the presence of methanol molecules in the interlayer space of methoxy–modified Kaol in the preparation steps appear to be crucial for the intercalation of CTMACl molecules and the subsequent swelling, delamination, and rolling of Kaol layers. The results from a supplementary experiment (not shown) indicate that kaolinites without surface methoxy modification, such as Kaol and Kaol–DMSO, were incapable of being intercalated with CTMACl and transformed into nanorolls. The intercalation of CTMACl also failed when Kaol–MeOH(dry) was used, which indicates that interlayer methanol molecules were indispensable for the intercalation of CTMACl. The methoxy-modified Kaol derived from N-methylformamide-intercalated Kaol as a precursor, like DMSO-intercalated Kaol, was also successfully used for the preparation of nanorolls (related results not shown). This indicates that the type of precursor used for the preparation of the methoxy-modified Kaol is relatively less important than the methoxy modification itself.

Increasing CTMACl-intercalation reaction temperatures did not obviously alter the XRD patterns of the products. As shown in Fig. S1 (see Supporting Information), the XRD patterns of CTMACl-modified Kaol (wet state, without ethanol washing) prepared at 30–100 °C are analogous to those of Kaol–CTMACl-30(unwashed). The *d* spacings at approximately 3.95, 1.96, and 1.30 nm are assigned respectively to the first-, second- and third-order reflections of the expanded lamellar structure in the walls of nanorolls. This result indicates that the overall pathway of the transformation from Kaol plate to nanoroll remained unchanged even though the CTMACl-intercalation reaction temperature changed.

The SSA and V_{por} values of the CTMACl-modified Kaol products gradually increase as the CTMACl-intercalation reaction temperatures rise, and the maximum values of SSA (57.3 m^2/g) and V_{por} (0.34 cm^3/g)

correspond to the intercalation temperature of 80 °C (Fig. 4b and c). The corresponding product, Kaol–CTMACl-80, exhibited a DRIFT spectrum (Fig. 5f) similar to that of Kaol–CTMACl-30 (Fig. 5e), which suggests that the overall pathway of the Kaol–nanoroll transformation in the two samples were alike.

The SSA and V_{por} values of the CTMACl-modified and calcined (at 600 °C) Kaol products were used to evaluate the effects of reaction temperatures because the organic species in the products were mostly decomposed and removed at 600 °C, and the lumens of the produced nanorolls were cleaned (the thermal behaviors of the CTMACl-modified Kaol are detailed in the Section 3.3), which avoids the influence of the remaining organic species on the porosity parameters. It is noteworthy that the calcined (at 600 °C) CTMACl-modified Kaol prepared at different intercalation temperatures present XRD patterns (not shown) similar to that of Kaol–CTMACl-30(600 °C) (Fig. 1g), which show broad diffraction maxima in response to the dehydroxylation of Kaol plates or nanorolls and the formation of an X-ray amorphous product. The SSA and V_{por} values of the calcined (600 °C) products of CTMACl-modified Kaol follow the same order as the uncalcined products (Fig. 4b and c). Kaol–CTMACl-80(600 °C) exhibits the maximum values of SSA (108.8 m^2/g) and V_{por} (0.45 cm^3/g), which suggests that the Kaol–nanoroll transformation is nearly optimized at the 80 °C CTMACl intercalation.

Promoting the Kaol–nanoroll transformation by increasing the intercalation reaction temperature is supported by TEM observation. For example, the coexistence of platy Kaol with nanorolls is readily seen in the TEM image of Kaol–CTMACl-30 (Fig. 3c), which shows that nanorolls became much more abundant than Kaol in the products as the CTMACl-intercalation temperature was above 60 °C. In particular, sample Kaol–CTMACl-80 shows the dominance of nanorolls in the TEM images (Fig. 6a). The PSD curve of Kaol–CTMACl-80 (the inset of Fig. 4a) shows a primary pore population centered at approximately 24.8 nm, which is analogous to that of Kaol–CTMACl-30. A minor distribution centered at approximately 17.6 nm is also shown in the PSD of Kaol–CTMACl-80, which represents the nanorolls produced with small diameters.

In addition to CTMACl-intercalation temperature, CTMACl concentration in reactant mixtures and reaction time also influence Kaol–nanoroll transformation. The preparation conditions of 1 M (CTMACl concentration) and 24 h (reaction time) were selected as the standard conditions based on the results of a series of preliminary experiments showing that a reaction time shorter than 24 h and CTMACl concentration lower than 1 M led to a decrease of SSA and V_{por} values. For example, the SSA and V_{por} values of Kaol–CTMACl-60 prepared with a reaction time of 6 h (CTMACl concentration = 1.0 M) are 45.8 m^2/g and 0.28 cm^3/g, respectively, and those of Kaol–CTMACl-60 prepared at 0.5 M (reaction time = 24 h) are 31.4 m^2/g and 0.17 cm^3/g, respectively. These values are lower than the SSA (46.5 m^2/g) and V_{por} (0.31 cm^3/g) values of Kaol–CTMACl-60 prepared under standard conditions (1 M CTMACl concentration and 24 h). Furthermore, it appears that a reaction time longer than 24 h and CTMACl concentration higher than 1 M did not obviously change the porosity data of the nanoroll products. For example, the SSA and V_{por} values of Kaol–CTMACl-100 prepared at a CTMACl concentration of 2.0 M are 49.9 m^2/g and 0.31 cm^3/g, respectively; those of the calcined (at 600 °C) product of this sample are 61.6 m^2/g and 0.33 cm^3/g, respectively. These values are substantially lower than those of their counterparts prepared under standard conditions (Fig. 4b and c). In the XRD pattern (Fig. S1) of Kaol–CTMACl-100(unwashed) (prepared at CTMACl concentration of 2.0 M), the diffractions with d spacings at 3.23 and 1.60 nm are shown. These diffractions are attributed to the solid CTMACl (Kuroda et al., 2011), which results from the crystallization of the CTMACl molecules. These results imply that the CTMACl molecules are in excess in this case. As a result, these molecules might occupy the pores of the produced nanorolls and lead to the decrease of porosity. The results discussed above suggest that CTMACl concentration and reaction time must be carefully adjusted for high volumes of Kaol–nanoroll transformation during the preparation of nanorolls.

A possible reason for the high Kaol–nanoroll transformation at the high CTMACl-intercalation temperature and CTMACl concentration is as follows. The diffusion of CTMACl into the interlayer region of the methoxy-modified Kaol might be accelerated at the high reaction temperature and CTMACl concentration, which produces more swelling Kaol particles and increases the initial materials available for the transformation. A similar mechanism has been demonstrated in the organosilane-

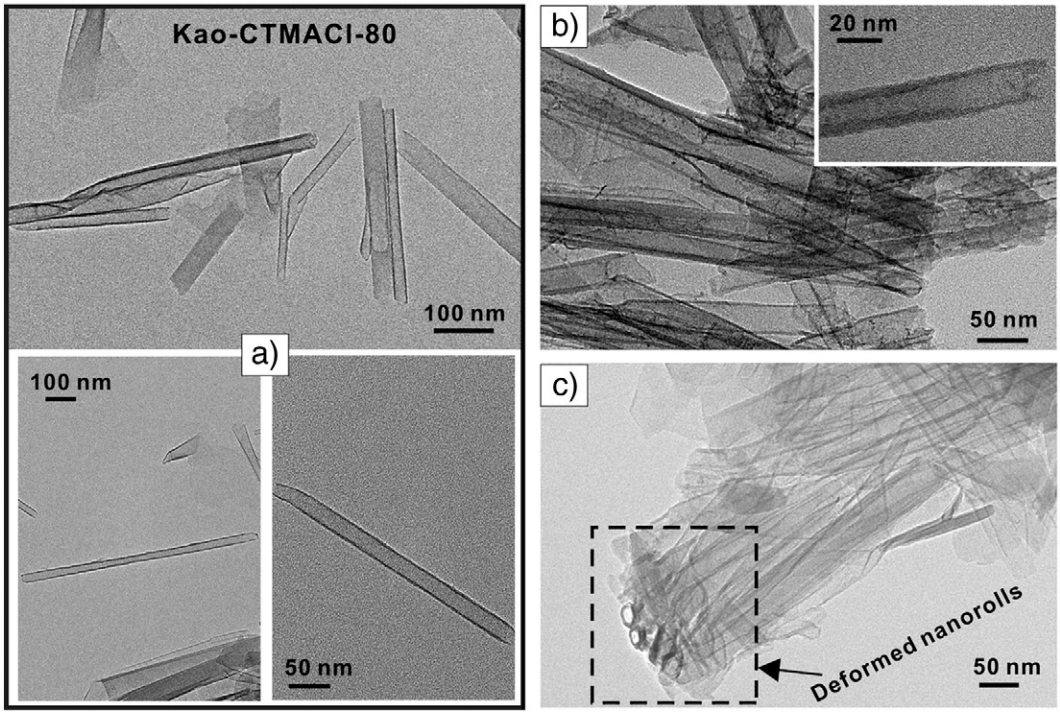

Fig. 6. TEM images of (a) Kaol–CTMACl-80; (b) Kaol–CTMACl-80(600 °C); (c) Kaol–CTMACl-80(900 °C).

modified Kaol, in which γ-aminopropyltriethoxysilane (APTES) was grafted in the interlayer space of Kaol (Yang et al., 2012). In that system, APTES used as solvent was found to be advantageous for the diffusion of APTES into the interlayer region (Tonle et al., 2007); a high temperature promoted the diffusion of APTES, which resulted in more grafting of APTES molecules in the interlayer aluminols. In addition, it is likely that the rolling of the Kaol plates was favored at high reaction temperatures such that more nanorolls were produced, but the exact mechanism is unclear because the related processes are difficult to monitor in real time.

3.3. Thermal stability of the nanorolls products under calcination

On the basis of the above results, Kaol–CTMACl-80 was used for thermal analyses because it is a product mainly composed of nanorolls. Three major steps of rapid mass loss were resolved in the TG curve of Kaol–CTMACl-80 (Fig. 7). The first is at 50–100 °C and corresponds to the DSC peak centered at approximately 60 °C; this step is ascribed to the removal of the physically adsorbed water or methanol molecules. The second, in the 200–300 °C range, corresponds to the DSC peak centered at approximately 258 °C (Fig. 7); this step is attributed to the removal of CTMACl molecules through combustion. The third mass-loss step at 300–600 °C, corresponding to the DSC endothermic peak centered at approximately 473 °C, is attributed to the dehydroxylation of the nanoroll. The decomposition and removal of the grafted methyl groups might also contribute to this mass loss. In the high–temperature range (800–1300 °C) of the DSC curve of Kaol–CTMACl-80, two exotherms occur at approximately 992 °C and 1250 °C (Fig. 7). These exotherms are attributable to the formation of γ-Al_2O_3 and the phase transformation from γ-Al_2O_3 and amorphous SiO_2 to mullite, respectively, according to previous reports on the structural changes of nanotubular halloysite under calcination (Smith et al., 1993; Yuan et al., 2012b). The exotherm at approximately 996 °C of natural kaolinite or halloysite has been comprehensively discussed in the literature; it is commonly understood that this reaction is triggered by the removal of the last hydroxyl groups and accompanied by the formation of a distinct alumina-rich phase. However, there is some debate about whether this alumina-rich phase is a spinel-like γ-Al_2O_3 or an alumina-rich mullite (Brindley and Lemaitre, 1987; Okada et al., 1986; Sonuparlak et al., 1987). Through a comprehensive ^{29}Si and ^{27}Al MAS NMR study, Smith et al. (1993) proposed that the exotherm at 996 °C of halloysite should be attributed to the formation of γ-Al_2O_3 on a very fine scale (<5 nm). This assumption is supported by Yuan et al. (2012b) in a study on the calcination of natural halloysite.

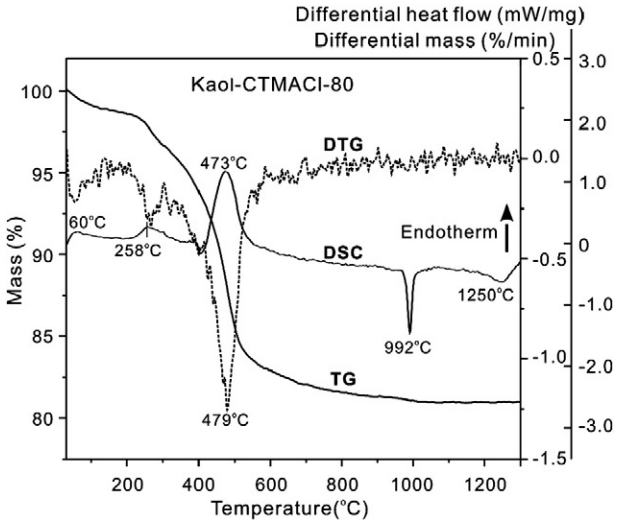

Fig. 7. TG, DTG, and DSC curves of Kaol–CTMACl-80.

The SSA and V_{por} values of Kaol–CTMACl-80(700 °C) are 88.6 m^2/g and 0.42 cm^3/g, respectively, which are obviously smaller than those of Kaol-CTMACl-80(600 °C). This result indicates that the destruction of the tubular structure of the produced nanorolls might have begun at 700 °C. Calcination at 800 °C and 900 °C further decreases the SSA and V_{por} values of the product (Fig. 4b and c), which indicates that structural destruction continues at these temperatures. As shown in Fig. 6b, calcination did not cause any obvious morphological changes in the nanorolls in Kaol–CTMACl-80(600 °C), but there was some slight morphological deformation and surface mottling of the nanoroll (inset of Fig. 6b). This phenomenon was also found in natural halloysite (Smith et al., 1993; Yuan et al., 2012b), and it was ascribed to the structural disordering associated with dehydroxylation and the phase separation of amorphous SiO_2 and Al_2O_3. The related reason was discussed in the studies described above. In the TEM image of Kaol–CTMACl-80(900 °C) (Fig. 6c), the distortions of nanorolls were more obvious, particularly some deformed nanorolls with twisted ends were observed (Fig. 6c). This result supports the changes of porosity data and indicates the destruction of the tubular structures of nanorolls.

In the DRIFT spectrum of Kaol–CTMACl-80(600 °C) (Fig. 5g), the hydroxyl group bands were significantly weakened, which indicates the dehydroxylation of the nanorolls that were produced. The vibration at 3216 cm^{-1} should be ascribed to N–H stretching of the remaining organics after calcination (Yang and Wei, 2001). In the DRIFT spectrum of the Kaol–CTMACl-80(700 °C) (Fig. 5h), a new band at 3745 cm^{-1} was resolved and assigned to the isolated surface silanols of amorphous silica (Morrow and Mcfarlan, 1992). A similar phenomenon was found in natural halloysite, and the 3745 cm^{-1} band was assigned to the isolated silanols, which were sourced from the amorphous silica expelled from the original Si–O tetrahedron (Yuan et al., 2012b). For Kaol–CTMACl-80(800 °C), the 3745 cm^{-1} band was more intense (Fig. 5i), which indicates the continued formation of amorphous silica. However, the 3745 cm^{-1} band was significantly decreased for Kaol-CTMACl-80(900 °C), which implies that the dehydroxylation of silanols had been mostly completed. It is noteworthy that previous study of Yuan et al. (2012b) demonstrated that the newly formed surface hydroxyl groups of calcined natural halloysite are available for organosilane grafting. Similarly, the availability of the surface hydroxyl groups of calcined nanorolls for organosilane modification could be postulated, which is important for the potential uses of nanorolls. First, the hydroxyl groups, or their silylated derivates, might act as new active sites for attracting and fixing functional guests. Second, the organo-modification of the external surface of calcined nanorolls permits the improvement of the affinity between the nanorolls and the polymer substrates in CPN.

These results show that the thermally induced changes of the nanorolls prepared through the delamination of Kaol resemble natural halloysite (Yuan et al., 2012b), but these nanorolls exhibit lower thermal stability than halloysite. For example, the endotherm peak related to the dehydroxylation in the DSC curve of Kaol–CTMACl-80 is centered at approximately 473 °C. This temperature is obviously lower than the dehydroxylation temperature (535 °C) of the initial Kaol (Yuan et al., 2008); it is also lower than the dehydroxylation temperature (519 °C) of natural halloysite (Yuan et al., 2012b). These results show that the prepared nanoroll is of lower structural order than halloysite and Kaol. For the same reason, the dehydroxylation of halloysite normally starts at a lower temperature than that of Kaol (Frost and Vassallo, 1996). Moreover, the prepared nanorolls have very thin walls (as previously described), which results in the proportion of the hydroxyl groups at the lumen surface being significantly higher than that in natural halloysite. These hydroxyl groups are not under the protection of tetrahedral and octahedral sheets and are thus more readily condensed via dehydroxylation than the hydroxyl groups on interlayer surfaces, which lower the dehydroxylation temperature.

In addition, the structural destruction of nanorolls began at approximately 700 °C; this process occurred at a significantly lower temperature than occurs with natural halloysite, which has a tubular structure

that remains unchanged at approximately 900 °C. This difference might be ascribed to the low structural order of nanorolls; in particular, the tube walls of nanorolls are thin, resulting in relatively low thermal persistence. On the other hand, the thin wall indicates a high delamination extent, which results in the high SSA and V_{por} values of the produced nanorolls. Thus, this property would be advantageous for the potential uses of nanorolls as adsorbents and fillers.

4. Conclusion

The transformation from platy Kaol into aluminosilicate nanorolls can be achieved through the simultaneous delamination and rolling of methoxy-modified Kaol as a result of the intercalation of CTMACl. The Kaol-nanoroll transformation efficiency was affected by the intercalation reaction parameters, including temperature, time, and CTMACl concentration. Among these parameters, intercalation temperature showed the most significant influence on the transformation. An increase of the CTMACl-intercalation temperature from 30 to 80 °C promoted the Kaol–nanoroll transformation resulting in an obvious increase in the specific surface area and porous volume values of the nanoroll products. The prepared aluminosilicate nanorolls are of low structural order with very thin tube walls. This dehydroxylation and thermally induced morphological changes of the Kaol-nanorolls occurred at lower temperatures than in naturally occurring halloysite.

Acknowledgments

Financial support from the Natural Scientific Foundation of China (Grant No. 41072032) and the Knowledge Innovation Program of the Chinese Academy of Sciences (Grant No. KZCX2-YW-QN101) are gratefully acknowledged. This is a contribution (no. IS-1720) from GIGCAS.

References

Annabi-Bergaya, F., Cruz, M.I., Gatineau, L., Fripiat, J.J., 1980. Adsorption of alcohols by smectites. III — Nature of the bonds. Clay Miner. 15, 225–237.
Bailey, S.W., 1989. Halloysite-a critical assessment. Sci. Géol. Mém. 86, 89–98.
Bates, T.F., Hildebrand, F.A., Swineford, A., 1950. Morphology and structure of endellite and halloysite. Am. Mineral. 35, 463–484.
Bobos, I., Duplay, J., Rocha, J., Gomes, C., 2001. Kaolinite to halloysite-7 Å transformation in the kaolin deposit of são vicente de pereira, Portugal. Clays Clay Miner. 49, 596–607.
Brindley, G.W., Lemaitre, J., 1987. Thermal, oxidation and reduction reactions of clay minerals. In: Newman, A.C.D. (Ed.), Chemistry of Clays and Clay Minerals. Longman Scientific & Technical, Harlow, pp. 319–370.
Churchman, G.J., Davy, T.J., Aylmore, L.A.G., Gilkes, R.J., Self, P.G., 1995. Characteristics of fine pores in some halloysites. Clay Miner. 30, 89–98.
Elaouar, M.A., 1962. The effect of temperature on clay minerals in aqueous suspension. Soc. Pet. Eng. J. 2, 216–222.
Frost, R.L., Vassallo, A.M., 1996. The dehydroxylation of the kaolinite clay minerals using infrared emission spectroscopy. Clays Clay Miner. 44, 635–651.
Frost, R.L., Kristof, J., Horvath, E., Kloprogge, J.T., 1999. Molecular structure of dimethyl sulfoxide in DMSO-intercalated kaolinites at 298 and 77 K. J. Phys. Chem. A 103, 9654–9660.
Gardolinski, J.E.F.C., Lagaly, G., 2005. Grafted organic derivatives of kaolinite: II. Intercalation of primary n-alkylamines and delamination. Clay Miner. 40, 547–556.
Giese, R.F., 1988. Kaolin minerals: structures and stabilities. Rev. Mineral. Geochem. 19, 29–66.
Gregg, S.J., Sing, K.S.W., 1982. Adsorption, surface area and porosity, 2nd ed. Academic Press, London.
Hedicke-Hochstotter, K., Lim, G.T., Altstadt, V., 2009. Novel polyamide nanocomposites based on silicate nanotubes of the mineral halloysite. Compos. Sci. Technol. 69, 330–334.
Johnston, C.T., Sposito, G., Bocian, D.F., Birge, R.R., 1984. Vibrational spectroscopic study of the interlamellar kaolinite—dimethyl sulfoxide complex. J. Phys. Chem. 88, 5959–5964.
Joussein, E., Petit, S., Churchman, J., Theng, B., Righi, D., Delvaux, B., 2005. Halloysite clay minerals - a review. Clay Miner. 40, 383–426.
Komori, Y., Sugahara, Y., Kuroda, K., 1999. Intercalation of alkylamines and water into kaolinite with methanol kaolinite as an intermediate. Appl. Clay Sci. 15, 241–252.
Komori, Y., Enoto, H., Takenawa, R., Hayashi, S., Sugahara, Y., Kuroda, K., 2000. Modification of the interlayer surface of kaolinite with methoxy groups. Langmuir 16, 5506–5508.
Kuroda, Y., Ito, K., Itabashi, K., Kuroda, K., 2011. One-step exfoliation of kaolinites and their transformation into nanoscrolls. Langmuir 27, 2028–2035.
Lagaly, G., 1981. Characterization of clays by organic-compounds. Clay Miner. 16, 1–21.
Lagaly, G., Ogawa, M., Dekany, M., 2006. Clay mineral organic interactions. In: Bergaya, F., Theng, B.K.G., Lagaly, G. (Eds.), Handbook of Clay Science. Elsevier, Amsterdam, pp. 309–377.
Letaief, S., Detellier, C., 2009. Clay-polymer nanocomposite material from the delamination of kaolinite in the presence of sodium polyacrylate. Langmuir 25, 10975–10979.
Levis, S.R., Deasy, P.B., 2002. Characterisation of halloysite for use as a microtubular drug delivery system. Int. J. Pharm. 243, 125–134.
Li, C.P., Liu, J.G., Qu, X.Z., Guo, B.C., Yang, Z.Z., 2008a. Polymer-modified halloysite composite nanotubes. J. Appl. Polym. Sci. 110, 3638–3646.
Li, Z.H., Jiang, W.T., Hong, H.L., 2008b. An FTIR investigation of hexadecyltrimethylammonium intercalation into rectorite. Spectrochim. Acta A Mol. Biomol. Spectrosc. 71, 1525–1534.
Lowell, S., Shields, J.E., Thomas, M.A., Thommes, M., 2004. Characterization of porous solids and powders: surface area, pore size and density. Kluwer Academic, Boston.
Lvov, Y.M., Shchukin, D.G., Mohwald, H., Price, R.R., 2008. Halloysite clay nanotubes for controlled release of protective agents. ACS Nano 2, 814–820.
Madejova, J., Komadel, P., 2001. Baseline studies of the clay minerals society source clays: infrared methods. Clays Clay Miner. 49, 410–432.
Martens, W.N., Frost, R.L., Kristof, J., Horvath, E., 2002. Modification of kaolinite surfaces through intercalation with deuterated dimethylsulfoxide. J. Phys. Chem. B 106, 4162–4171.
Matusik, J., Gawel, A., Bielanska, E., Osuch, W., Bahranowski, K., 2009. The effect of structural order on nanotubes derived from kaolin-group minerals. Clays Clay Miner. 57, 452–464.
Morrow, B.A., Mcfarlan, A.J., 1992. Surface vibrational-modes of silanol groups on silica. J. Phys. Chem. 96, 1395–1400.
Okada, K., Otsuka, N., Ossaka, J., 1986. Characterization of spinel phase formed in the kaolin-mullite thermal sequence. J. Am. Ceram. Soc. 69, C251–C253.
Pasbakhsh, P., Churchman, G.J., Keeling, J.L., 2013. Characterisation of properties of various halloysites relevant to their use as nanotubes and microfibre fillers. Appl. Clay Sci. 74, 47–57.
Rathman, J.F., Scheuing, D.R., 1990. Alkyldimethylamine oxide surfactants. In: Scheuing, D.R. (Ed.), Fourier transform infrared spectroscopy in colloid and interface scienceAmerican Chemical Society 123–142.
Raupach, M., Barron, P.F., Thompson, J.G., 1987. Nuclear-magnetic-resonance, infrared, and X-ray-powder diffraction study of dimethylsulfoxide and dimethylselenoxide intercalates with kaolinite. Clays Clay Miner. 35, 208–219.
Shchukin, D.G., Sukhorukov, G.B., Price, R.R., Lvov, Y.M., 2005. Halloysite nanotubes as biomimetic nanoreactors. Small 1, 510–513.
Singh, B., 1996. Why does halloysite roll? — a new model. Clays Clay Miner. 44, 191–196.
Singh, B., Gilkes, R.J., 1992. An electron-optical investigation of the alteration of kaolinite to halloysite. Clays Clay Miner. 40, 212–229.
Singh, B., Mackinnon, I.D.R., 1996. Experimental transformation of kaolinite to halloysite. Clays Clay Miner. 44, 825–834.
Smith, M.E., Neal, G., Trigg, M.B., Drennan, J., 1993. Structural characterization of the thermal transformation of halloysite by solid-state NMR. Appl. Magn. Reson. 4, 157–170.
Sonuparlak, B., Sarikaya, M., Aksay, I.A., 1987. Spinel phase formation during the 980 °C exothermic reaction in the kaolinite-to-mullite reaction series. J. Am. Ceram. Soc. 70, 837–842.
Tan, D.Y., Yuan, P., Annabi-Bergaya, F., Yu, H.G., Liu, D., Liu, H.M., He, H.P., 2013. Natural halloysite nanotubes as mesoporous carriers for the loading of ibuprofen. Microporous Mesoporous Mater. 179, 89–98.
Thompson, J.G., Cuff, C., 1985. Crystal-structure of kaolinite: dimethylsulfoxide intercalate. Clays Clay Miner. 33, 490–500.
Tonle, I.K., Diaco, T., Ngameni, E., Detellier, C., 2007. Nanohybrid kaolinite-based materials obtained from the interlayer grafting of 3-aminopropyltriethoxysilane and their potential use as electrochemical sensors. Chem. Mater. 19, 6629–6636.
Tunney, J., Detellier, C., 1994. Preparation and characterization of an 8.4-angstrom hydrate of kaolinite. Clays Clay Miner. 42, 473–476.
Tunney, J.J., Detellier, C., 1996. Chemically modified kaolinite. Grafting of methoxy groups on the interlamellar aluminol surface of kaolinite. J. Mater. Chem. 6, 1679–1685.
Van Oss, C.J., Naim, J.O., Costanzo, P.M., Giese, R.F., Wu, W., Sorling, A.F., 1999. Impact of different asbestos species and other mineral particles on pulmonary pathogenesis. Clays Clay Miner. 47, 697–707.
Vergaro, V., Abdullayev, E., Lvov, Y.M., Zeitoun, A., Cingolani, R., Rinaldi, R., Leporatti, S., 2010. Cytocompatibility and uptake of halloysite clay nanotubes. Biomacromolecules 11, 820–826.
Yang, C.P., Wei, C.S., 2001. Synthesis and properties of soluble alternating copoly(amide–imide)s based on 1,2-bis(4-trimellitimidophenoxy)-4-t-butylbenzene and various aromatic diamines. Polymer 42, 1837–1848.
Yang, S.Q., Yuan, P., He, H.P., Qin, Z.H., Zhou, Q., Zhu, J.X., Liu, D., 2012. Effect of reaction temperature on grafting of gamma-aminopropyl triethoxysilane (APTES) onto kaolinite. Appl. Clay Sci. 62–63, 8–14.
Yuan, P., Southon, P.D., Liu, Z.W., Green, M.E.R., Hook, J.M., Antill, S.J., Kepert, C.J., 2008. Functionalization of halloysite clay nanotubes by grafting with γ-aminopropyltriethoxysilane. J. Phys. Chem. C 112, 15742–15751.
Yuan, P., Southon, P.D., Liu, Z.W., Kepert, C.J., 2012a. Organosilane functionalization of halloysite nanotubes for enhanced loading and controlled release. Nanotechnology 23, 375705.
Yuan, P., Tan, D.Y., Annabi-Bergaya, F., Yan, W.C., Fan, M.D., Liu, D., He, H.P., 2012b. Changes in structure, morphology, porosity, and surface activity of mesoporous halloysite nanotubes under heating. Clay Clay Miner. 60, 557–569.
Zeng, Q.H., Yu, A.B., Lu, G.Q., Standish, R.K., 2003. Molecular dynamics simulation of organic-inorganic nanocomposites: layering behavior and interlayer structure of organoclays. Chem. Mater. 15, 4732–4738.
Zhou, C.H., Keeling, J., 2013. Fundamental and applied research on clay minerals: From climate and environment. Appl. Clay Sci. 74, 3–9.